

pubs.acs.org/NanoLett Letter

High-Contrast Plasmonic-Enhanced Shallow Spin Defects in Hexagonal Boron Nitride for Quantum Sensing

Xingyu Gao, Boyang Jiang, Andres E. Llacsahuanga Allcca, Kunhong Shen, Mohammad A. Sadi, Abhishek B. Solanki, Peng Ju, Zhujing Xu, Pramey Upadhyaya, Yong P. Chen, Sunil A. Bhave, and Tongcang Li*



Cite This: https://doi.org/10.1021/acs.nanolett.1c02495



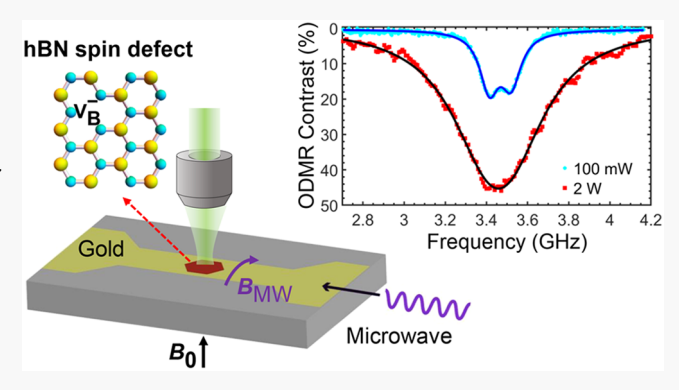
ACCESS

Metrics & More

Article Recommendations

Supporting Information

ABSTRACT: The recently discovered spin defects in hexagonal boron nitride (hBN), a layered van der Waals material, have great potential in quantum sensing. However, the photoluminescence and the contrast of the optically detected magnetic resonance (ODMR) of hBN spin defects are relatively low so far, which limits their sensitivity. Here we report a record-high ODMR contrast of 46% at room temperature and simultaneous enhancement of the photoluminescence of hBN spin defects by up to 17-fold by the surface plasmon of a gold film microwave waveguide. Our results are obtained with shallow boron vacancy spin defects in hBN nanosheets created by low-energy He⁺ ion implantation and a gold film microwave waveguide fabricated by photolithography. We also explore the effects of microwave and laser powers on the ODMR



and improve the sensitivity of hBN spin defects for magnetic field detection. Our results support the promising potential of hBN spin defects for nanoscale quantum sensing.

KEYWORDS: spin defects, hexagonal boron nitride, quantum sensing, optically detected magnetic resonance

ptically active spin defects in wide-band-gap materials have shown great potential for a wide range of emerging technologies, from quantum information processing^{1,2} to high-resolution sensing of magnetic and electric fields.^{3–6} Color centers in bulk semiconductors such as diamond^{7,8} and silicon carbide^{9,10} are prime examples that reveal optically detected magnetic resonance (ODMR). Recently, atomic defects in layered van der Waals materials such as hexagonal boron nitride (hBN) are attracting increasing attention as alternative candidates for studying light—matter interaction, nanophotonics, and nanoscale sensing. $^{11-14}$ Atomic defects in hBN are stable in nanosheets as thin as a monolayer and are readily accessible for device integration and top down nanofabrication. 15,16 Furthermore, recent experiments discovered that some defects in hBN could be spin addressable at room temperature. 17-22 The negatively charged boron vacancy (V_B⁻) spin defect is the most studied one among these defects. $^{23-25}$ It has spin s=1, and its orientation is out of plane. V_B defects can be generated by neutron irradiation, 17,26 ion implantation, 27 femtosecond laser writing, 28 and electron irradiation.²⁹ Spin defects in thin hBN nanosheets will be useful for quantum sensing and spin optomechanics.^{30,31} However, so far, the $V_{\rm B}^{-}$ spin defects have relatively low brightness and ODMR contrast, which limits their sensitivity in quantum sensing.22

Here we report high-contrast plasmonic-enhanced shallow $V_{\rm B}^{-}$ spin defects in hBN nanosheets for quantum sensing. We fabricate a gold film coplanar microwave waveguide by photolithography to optimize the homogeneity and local intensity of the microwave for spin control. The hBN nanosheets with spin defects are transferred onto the microwave waveguide and are in contact with the gold surface for both plasmonic emission enhancement and spin control. The surface plasmons³²⁻³⁴ provide broadband emission enhancement covering the wide range of the photoluminescence (PL) of V_B^- defects from 750 to 950 nm. Our method does not require complex nanofabrication or cause adverse effects on quantum sensing. The microwave magnetic field generated by the gold waveguide is parallel to the surface and perpendicular to the orientation of $V_{\rm B}^-$ electron spins, which is crucial to achieve high ODMR contrast. With these, we find that the ODMR contrast can reach 46% at room temperature,

Received: June 28, 2021 Revised: August 25, 2021



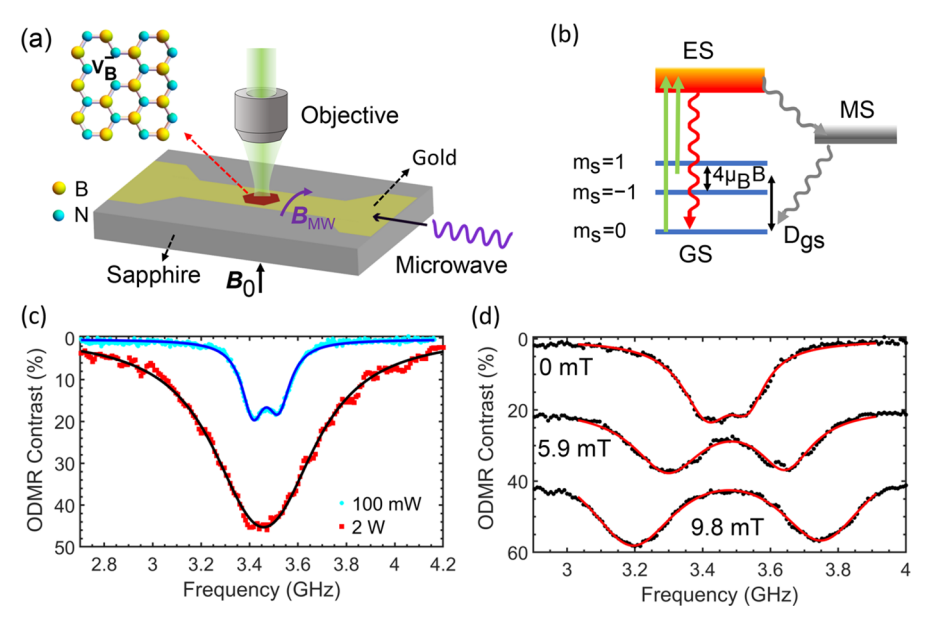


Figure 1. (a) An illustration of the experimental setup for ODMR measurements. An ion implanted hBN nanosheet is placed on top of a gold film microwave stripline. A microwave is delivered through the stripline for spin manipulation. The surface plasmon of the gold surface provides emission enhancement. An NA = 0.9 objective lens is used to excite V_B^- defects with a 532 nm laser and collect the PL. A permanent magnet is used to apply a static magnetic field. (b) The energy diagram of a V_B^- defect and the optical pumping cycle between the ground state (GS), the excited state (ES), and the metastable state (MS). A magnetic field induces Zeeman shifts of the spin sublevels. (c) Measured CW ODMR spectra under 100 mW (light blue dots) and 2 W (red squares) microwave driving. With a high-power microwave (2 W), the ODMR contrast can reach 46%. The laser excitation power is 5 mW. The V_B^- defects are generated by 2.5 keV He⁺ ion implantation. (d) ODMR spectra in different external magnetic fields. A clear splitting of 346 and 560 MHz is observed in 5.9 and 9.8 mT magnetic fields, respectively. Solid curves are fittings with a double Lorentzian model.

which is an order of magnitude larger than the highest room-temperature ODMR contrast of hBN spin defects reported in the previous work. We also observe an up to 17-fold photoluminescence (PL) enhancement of $V_{\rm B}^-$ defects due to the gold film. We measure the spin initialization time to be around 100 ns. In addition, we study the laser power and microwave power dependence of the continuous-wave (CW) ODMR and optimize the magnetic field sensitivity to be about 8 $\mu T/\sqrt{Hz}$. Finally, we perform coherent spin control and measure the spin—lattice relaxation time T_1 and the spin coherence time T_2 of $V_{\rm B}^-$ spin defects generated by He⁺ ion implantation, which can benefit future works on multipulse sensing protocols. Our results demonstrate the promising potential of shallow hBN spin defects for nanoscale quantum sensing and other quantum technologies.

The results presented in this work are obtained with tapeexfoliated hBN nanosheets which are tens of nanometers thick. We exfoliate hBN flakes onto a Si wafer and then mount the wafer in a home-built ion implanter for doping. We use lowenergy He⁺ ions (200 eV to 3 keV) to implant hBN nanosheets, which creates high-quality $V_{\rm B}^{-}$ defects with average depths ranging from 3 to 30 nm and avoids introducing undesired defects.³⁶ After ion implantation, the hBN flakes are transferred onto a gold microwave stripline on a sapphire substrate and characterized using an ODMR setup (Figure 1a). CW ODMR measurements are performed to acquire the basic spin properties of the $V_{\rm B}^{-}$ defects generated by He⁺ ions. The defects are excited by a 532 nm laser with an NA = 0.9 objective lens, which also collects the PL of defects. We record integrated photon counts as a function of the applied microwave. We obtain the difference between the photon count rates when the microwave is off (I_{off}) and when the microwave is on (I_{on}) . The ODMR contrast is then determined by normalizing the PL difference with the PL intensity when the microwave is off: $C = (I_{\rm off} - I_{\rm on})/I_{\rm off}$. A positive ODMR contrast C means that the microwave driving decreases the PL intensity. The energy level structure of $V_{\rm B}^-$ defects in hBN is shown in Figure 1b.

Figure 1c shows measured high-contrast ODMR spectra of $V_{\rm B}^{-}$ defects at room temperature. Strikingly, with strong microwave driving, we find that these defects can exhibit up to 46% ODMR contrast, which is 1 order of magnitude higher than the best contrast of hBN spin defects reported previously.³⁵ This value is even larger than the ODMR contrast of diamond nitrogen-vacancy centers at room temperature.⁷ The ODMR contrast can readily reach around 20% without significant power broadening using low-power microwave driving. We also observe a similar high contrast with a thick hBN flake on the gold stripline which does not show PL enhancement (Supporting Information, Figure S7). It is noted that such a high ODMR contrast is due to the good alignment of the microwave magnetic driving field and the strong driving field strength. Since the hBN flakes are placed directly on the gold stripline, the driving magnetic field is parallel to its surface and perpendicular to the $V_{\rm B}^-$ spins, which yields the maximum ODMR contrast. In comparison, for a hBN flake placed inside a Ω -shaped waveguide, we observe a 6fold lower ODMR contrast with the same microwave power (Supporting Information, Figure S6). The decrease of the ODMR contrast is due to the misalignment of the driving microwave magnetic field, which is nearly out of plane inside a Ω -shaped ring.

Without an external magnetic field, the measured ODMR spectrum shows two resonances at ν_1 and ν_2 centered around ν_0 (Figure 1c). The results agree well with a double Lorentzian model. Here ν_0 is determined by the zero-field splitting (ZFS),

 $\nu_0=D_{\rm gs}/h=3.47$ GHz, where h is the Planck constant. And the splitting between ν_1 and ν_2 is due to the nonzero off-axial ZFS parameter $E_{\rm gs}/h=50$ MHz. Figure 1d presents ODMR spectra in different external static magnetic fields. We use a permanent magnet to apply a static magnetic field perpendicular to the nanosheet surface. A translation stage is used to change the position of the magnet and tune the magnetic field strength. With an external static magnetic field B, ν_1 and ν_2 will be split further owing to the Zeeman effect, $\nu_{1,2}=D_{\rm gs}/h\pm\sqrt{E_{\rm gs}^2+(g\mu_{\rm B}B)^2}/h$, where g=2 is the Landé g-factor. The splitting $(\nu_2-\nu_1)$ is 560 MHz (346 MHz) at 9.8 mT (5.9 mT).

It is highly desirable to create spin defects as close to the surface as possible without degrading the spin properties for nanoscale quantum sensing. This can decrease the ultimate distance between a sample and the sensor, which can significantly improve the signal. In Figure 2, we study the

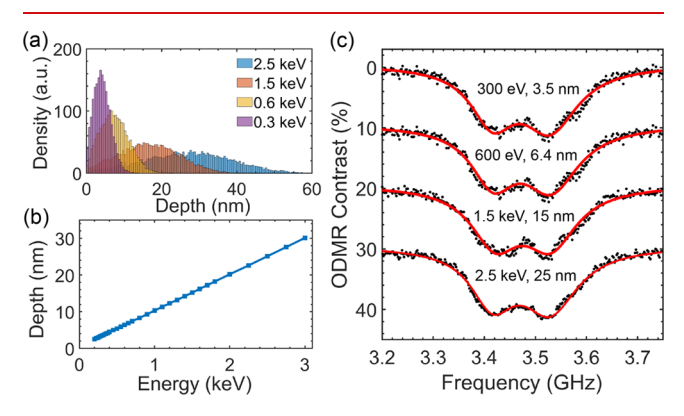


Figure 2. (a) The depth distribution of defects created by He $^+$ ions with different implantation energies. The results are obtained with SRIM simulation. (b) The most probable depth to create defects as a function of ion energies. (c) Measured ODMR spectra of V_B^- with different implantation depths. The line widths are 122, 115, 104, and 103 MHz for 3.5, 6.2, 15, and 25 nm depths, respectively.

formation of shallow $V_{\rm B}^-$ defects by using He⁺ ions. First, we use the Stopping and Range of Ions in Matter (SRIM) software to calculate the depths and densities of vacancies created with different ion energies from 200 eV to 3 keV (Figure 2a,b). The most probable depth is 3.5, 6.4, 15, and 25 nm when the He⁺ ion energy is 300 eV, 600 eV, 1.5 keV, and 2.5 keV, respectively. Then, we perform the CW ODMR measurements on the samples with different doping depths. Here we use weak microwave driving to avoid the power broadening. Therefore, we can extract the nature linewidth of $V_{\rm B}^-$ defects (Figure 2c). All of the ODMR spectra display similar line widths as well as the contrasts, indicating the hBN spin properties are nearly the same at different doping depths.

For sensing applications, the PL brightness is an important factor that directly affects the sensitivity. Former theoretical studies indicate that the near-infrared optical transition of $V_{\rm B}^{-}$ defects is not an electric-dipole-allowed transition and is hence relatively dark. In this context, improving their brightness is a crucial task. Here we utilize surface plasmons of a metallic film $^{32-34}$ to enhance the brightness of the $V_{\rm B}^{-}$. Surface plasmons are collective oscillations of coupled eletromagnetic waves and free electrons on metallic surfaces. They have large localized electric and magnetic fields which can speed up both radiative and non-radiative decays. We chose plasmonic

enhancement because it can cover the whole broad PL spectral range of $V_{\rm B}^{-}$ defects. In addition, this method can utilize the metallic surface of our microwave waveguide and does not require complex nanofabrication. Our microwave waveguide is made of a 300 nm thick gold film prepared by electron-beam physical vapor deposition on top of a sapphire wafer. The width of the center microstrip is 50 μ m. The hBN flakes with $V_{\rm B}^{-}$ defects are transferred onto both the gold film and the sapphire substrate for comparison (Figure 3a). V_B^- defects on both gold and sapphire surfaces display broad PL emission spectra around 810 nm (Figure 3b). Remarkably, the $V_{\rm B}$ defects on the gold film show an order of magnitude higher PL intensity than those on the sapphire substrate under the same laser excitation. Parts c and d of Figure 3 present the PL intensities of these two samples and their PL ratio at different laser excitation powers. The experimental data in Figure 3c are fit to $I = I_{\text{sat}}/(1 + P_{\text{sat}}/P_{\text{laser}})$, where I is the PL intensity of the $V_{\rm B}^{-}$, $I_{\rm sat}$ is the saturation PL intensity, $P_{\rm laser}$ is the excitation laser power, and P_{sat} is the saturation laser power. On a gold film, the $V_{\rm B}^{-}$ defects show up to 17-fold enhancement of PL intensities under low-power excitation. We also observe a strong modification of the saturation behavior (Figure 3c). The laser saturation power P_{sat} is reduced by a factor of 5, and the saturation PL count rate I_{sat} is increased by around 3.5 times. These indicate that a gold film can improve the quantum efficiency of $V_{\rm B}^-$ defects significantly.

We also study the effect of the separation between the gold film and $V_{
m B}^-$ defects on the brightness enhancement. We transfer hBN flakes with different thickness onto the gold micostrip, so that we can get various distances between the V_B defects and the gold film. The thickness of hBN nanosheets is measured by an atomic force microscope (AFM). The PL intensities are measured before and after transfer. Here we use 600 eV He^+ ions to generate shallow V_B^- with a most probable depth of 6.4 nm. Therefore, the average separation between the gold film and V_B^- defects is equal to the thickness of hBN nanosheets subtracted by 6.4 nm. As a result, we observe a strong thickness dependence of the PL enhancement. The highest enhancement is obtained when the hBN flake thickness is around 32 nm (Figure 3e). Our result is consistent with the former result on plasmonic enhancement of quantum dots on a gold surface.³³ When a hBN nanosheet is too thin, the nonradiative decay dominates. There is also little brightness enhancement when the hBN nanosheet is too thick because the surface plasmonic modes decay exponentially away from the surface. Thus, there is an optimal thickness for plasmonic enhancement. In addition, we characterize the electron spin initialization time of V_B^- defects on both gold and sapphire surfaces as a function of the power of the 532 nm excitation laser (see the Supporting Information for more details). We find that the required spin initialization time can be about 100 ns under high-power excitation (Figure 3f). Thus, the groundstate recovery time should be less than 100 ns, which is much shorter than the former theoretical prediction.²⁵ Our results may be helpful for future theoretical works on $V_{\rm B}^{-}$ spin defects. The gold film reduces the spin initialization time (Figure 3f), which also speeds up quantum sensing.

Sensitivity is the most important parameter to determine the performance of a sensor. To measure an external static magnetic field with spin defects, a common way is to use CW ODMR to detect the Zeeman shifts of the spin sublevels caused by the magnetic field.⁵ The precision to determine the magnetic field is directly affected by the photon count rate *R*,

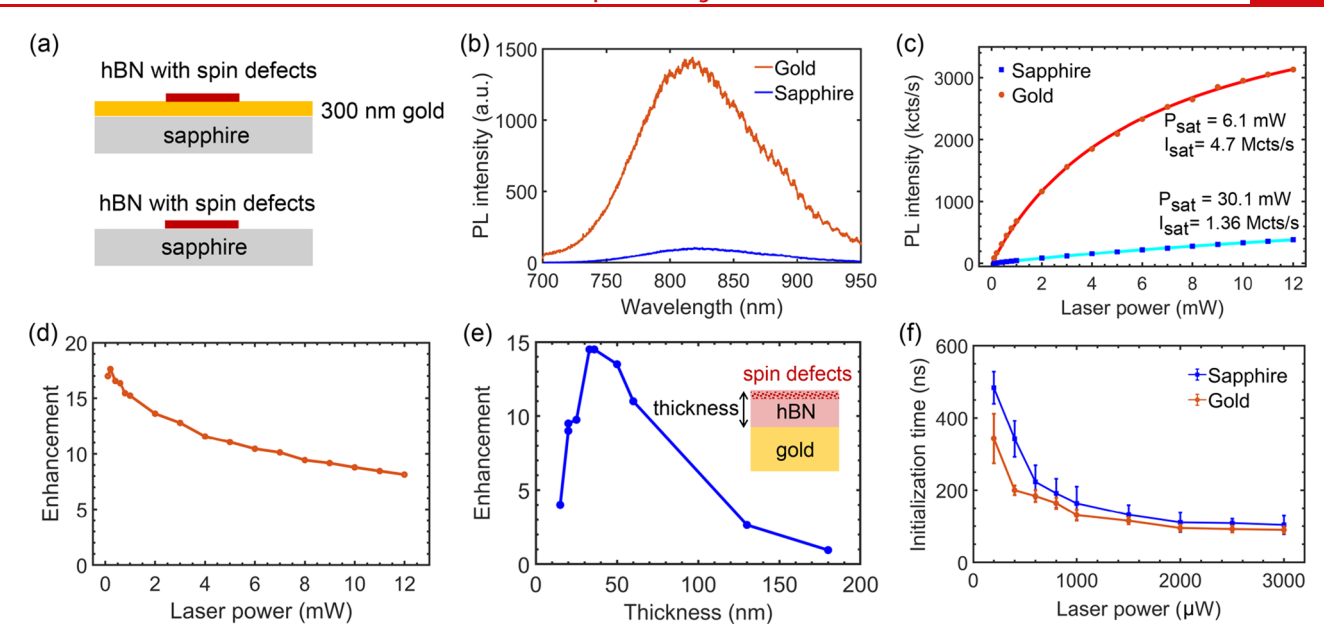


Figure 3. (a) Illustrations of hBN nanosheets with spin defects on top of a 300 nm-thick gold film and on top of a bare sapphire wafer for comparison. (b) A comparison of the PL spectra of V_B^- defects on a gold film and on a sapphire substrate. The gold film enhances the PL count rate substantially. The V_B^- defects are generated by 2.5 keV He⁺ ions. (c) PL intensities of V_B^- defects on a gold film and a sapphire substrate as functions of the laser power. (d) PL enhancement at different laser powers. The enhancement is obtained by calculating the ratio of PL intensities of the V_B^- defects on the gold film and the sapphire substrate. The enhancement is up to 17 when the laser power is low. (e) Dependence of the PL enhancement on the thickness of the hBN nanosheet. The highest PL enhancement is obtained when the thickness is around 35 nm. The V_B^- defects are generated by 600 eV He⁺ ions and are near the top surface of the hBN nanosheet. (f) The required time for optically polarizing V_B^- electron spins as a function of the laser power.

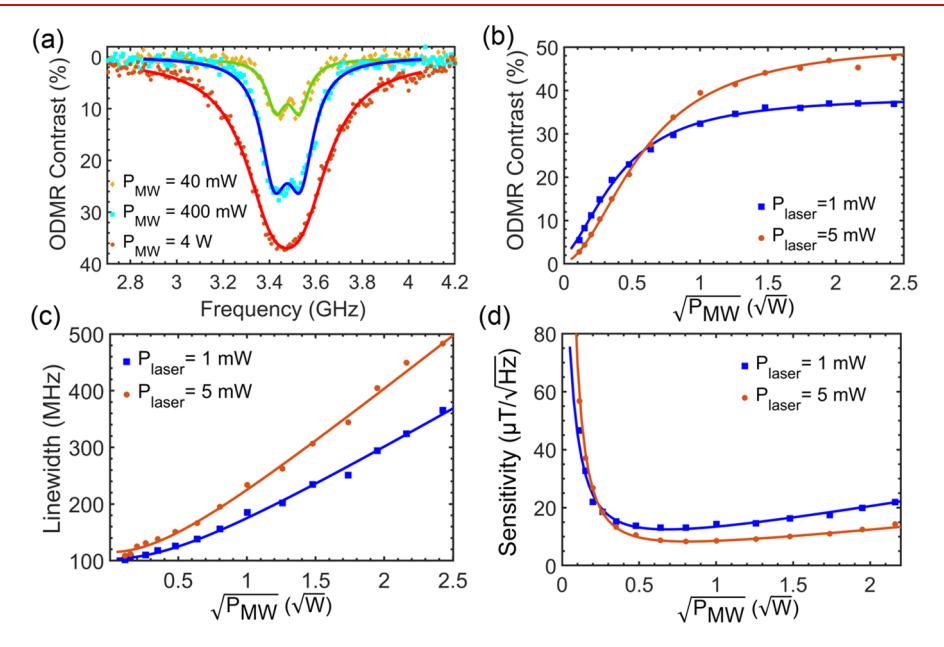


Figure 4. (a) Typical CW ODMR spectra of V_B^- spin defects at different microwave powers. The laser excitation power is 1 mW. No external magnetic field is applied. (b) ODMR peak contrast as a function of the microwave power. (c) Microwave power dependence of the ODMR linewidth. (d) Magnetic field sensitivity as a function of the microwave power. The orange dots and blue squares are experimental data. Solid curves are fittings with theoretical models.

the ODMR contrast C, and the linewidth $\Delta \nu$, following the equation³⁷

$$\eta_{\rm B} = A \times \frac{h}{g\mu_{\rm B}} \times \frac{\Delta\nu}{C\sqrt{R}} \tag{1}$$

where μ_B is the Bohr magneton. In this expression, A is a numerical parameter related to the specific line shape function.

For a Lorentzian profile, $A \approx 0.77$. The values of C, $\Delta \nu$, and R are further related to the microwave power and laser power³⁷ (see the Supporting Information). To improve the detection sensitivity, it is crucial to increase the count rate and contrast as high as possible without significant power broadening of the linewidth.

Here we perform a group of CW ODMR measurements with various microwave powers and laser powers to find the

optimal conditions for magnetic field sensing (Figure 4). Figure 4a presents three typical CW ODMR spectra at different microwave powers. Under low-power 40 mW microwave driving, we obtain an ODMR contrast of ~10%. Such a low microwave power does not induce significant spectral power broadening. A natural linewidth can be extracted as ~110 MHz. With an increasing microwave power, we first observe a significant improvement of the contrast without much spectral broadening. When we increase the microwave power further, the linewidth broadening becomes severe. Parts b-d of Figure 4 present the quantitative measurements of the ODMR contrast, linewidth, and sensitivity as functions of the microwave power. The experimental results fit well with theoretical models, as discussed in the Supporting Information. Here we perform the experiments at two different laser powers (1 and 5 mW). The 5 mW laser excitation gives a broader linewidth but a higher saturation ODMR contrast compared to those with 1 mW laser excitation. As a result, if we increase the microwave power, the sensitivity is first improved owing to the increase of the ODMR contrast and then becomes worse when the spectral power broadening dominates. The best sensitivity that we have achieved is about 8 $\mu T/\sqrt{Hz}$. This sensitivity is 10 times better than the former result with hBN spin defects (our system also has a better spatial resolution).²² This sensitivity will be enough for studying many interesting phenomena in magnetic materials. For example, the magnetic field generated by a monolayer CrI₃ (a 2D van der Waals magnet) is on the order of 200 μ T.

Finally, we perform pulsed ODMR measurements to determine the spin-lattice relaxation time T_1 and the spin coherence time T_2 of the shallow V_B^- defects generated by ion implantation. T_1 and T_2 of hBN spin defects have only been measured for neutron irradiated samples before. 19,26 It will be useful to know their values for our shallow spin defects created by ion implantation. In addition, pulsed ODMR measurements are inevitable steps for realizing more complex sensing protocols. A pulsed ODMR measurement consists of optical initialization of the ground state, coherent manipulation of the spin state with microwave pulses, and optical readout of the final spin state. Here we add an external magnetic field of 13 mT to split two branches of the V_B^- spin sublevels. $m_s = 1,0$ states are used as the two-level spin system to carry out the spin coherent control. Figure 5a shows the Rabi oscillation as a function of the microwave power. The data is fit using $A + B_1$ $\exp(-\tau T_{2,1}^*) \cos(2\pi f_1 \tau + \phi_1) + B_2 \exp(-\tau/T_{2,2}^*) \cos(2\pi f_2 \tau + \phi_2)$ ϕ_2). We observe an oscillation with two Rabi frequencies, which are in the tens of megahertz range. The exponential decay of one oscillation component gives the spin-dephasing time of T_2^* = 120 ns. To gain more insight into the spin properties of the $V_{\rm B}^-$ defects at different depths, we measure the spin-lattice relaxation times T_1 and spin-spin relaxation times T_2 of the V_B^- defects created with different ion implantation energies. The pulse sequences are shown as insets in the left panels of Figure 5b,c. By fitting the results, T_1 and T_2 are obtained as ~17 and ~1.1 μ s, respectively. As shown in Figure 5b,c, both T_1 and T_2 are independent of the ion energy, indicating the spin properties of the $V_{\rm B}^-$ defects are nearly independent of the depth. The depth-independent T_2 suggests that the coherence times are not limited by the surface. They are likely dominated by nuclear spin noise but

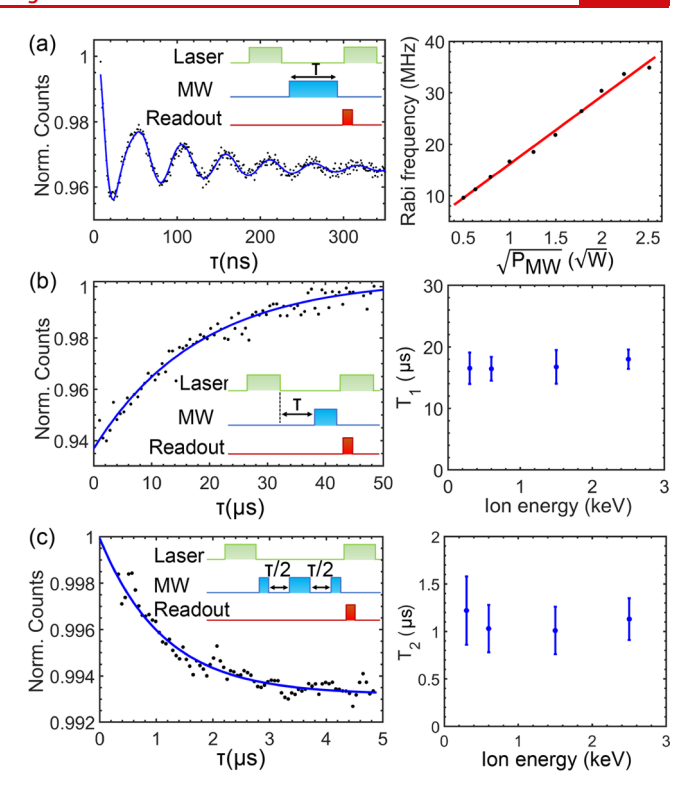


Figure 5. Pulsed ODMR measurements of $V_{\rm B}^-$ spin defects. A static magnetic field of 13 mT perpendicular to the hBN nanosheet is applied to split the spin sublevels. (a) (left panel) Rabi oscillation of $V_{\rm B}^-$ spin defects. (right panel) Rabi frequency as a function of the microwave power. (b) (left panel) Measurement of the spin—lattice relaxation time T_1 . (right panel) T_1 of T_1 defects with different depths. (c) (left panel) Measurement of the spin—spin relaxation time T_2 . (right panel) T_2 of the T_2 defects with different depths.

may also be limited by the inhomogeneity, as we use an ensemble of spin defects instead of a single spin defect.³⁸

In conclusion, we have realized a significant improvement of the ODMR contrast and the brightness of hBN V_B^- spin defects. We observe a record-high ODMR contrast of 46%, which is 1 order of magnitude higher than the best former result with hBN. We use low-energy He+ ion implantation to create $V_{\rm B}^{-}$ defects as shallow as 3 nm in hBN nanosheets. Moreover, both CW and pulsed ODMR measurements display that their spin properties are nearly independent of the ion implantation energy. This result confirms the feasibility to create high-quality $V_{\rm B}^-$ defects proximal to the hBN surface. In addition, we utilize the gold film surface plasmon to enhance the brightness of $V_{\rm B}^-$ defects and obtain an up to 17-fold enhancement of the PL intensity. We also explore the effects of laser power and microwave power on the CW ODMR contrast and linewidth. With these, we achieve a CW ODMR sensitivity around 8 $\mu T/\sqrt{Hz}$. We expect that the PL can be enhanced further with plasmonic nanoantennas,³⁹ and the magnetic field sensitivity can be improved by using more powerful pulsed sensing protocols. In addition, during the preparation of this manuscript, we became aware of a related work 40 that reported a PL enhancement of hBN spin defects with a photonic cavity by a factor of ~6 at high NA collection and an ODMR contrast of about 5%. The surface plasmon may be combined with a photonic cavity to obtain better results in the future. Our work strongly supports the promising potential of V_B^- defects as a nanoscale sensor in a 2D material platform.

ASSOCIATED CONTENT

5 Supporting Information

The Supporting Information is available free of charge at https://pubs.acs.org/doi/10.1021/acs.nanolett.1c02495.

Additional experimental details, methods, analysis of results, and figures of photoluminescence intensities and ODMR contrasts (PDF)

AUTHOR INFORMATION

Corresponding Author

Tongcang Li — Department of Physics and Astronomy, Purdue University, West Lafayette, Indiana 47907, United States; Elmore Family School of Electrical and Computer Engineering, Birck Nanotechnology Center, and Purdue Quantum Science and Engineering Institute, Purdue University, West Lafayette, Indiana 47907, United States; orcid.org/0000-0003-3308-8718; Email: tcli@purdue.edu

Authors

- Xingyu Gao Department of Physics and Astronomy, Purdue University, West Lafayette, Indiana 47907, United States
- Boyang Jiang Elmore Family School of Electrical and Computer Engineering, Purdue University, West Lafayette, Indiana 47907, United States
- Andres E. Llacsahuanga Allcca Department of Physics and Astronomy, Purdue University, West Lafayette, Indiana 47907, United States
- Kunhong Shen Department of Physics and Astronomy, Purdue University, West Lafayette, Indiana 47907, United States
- Mohammad A. Sadi Elmore Family School of Electrical and Computer Engineering, Purdue University, West Lafayette, Indiana 47907, United States
- Abhishek B. Solanki Elmore Family School of Electrical and Computer Engineering, Purdue University, West Lafayette, Indiana 47907, United States
- Peng Ju Department of Physics and Astronomy, Purdue University, West Lafayette, Indiana 47907, United States
- **Zhujing Xu** Department of Physics and Astronomy, Purdue University, West Lafayette, Indiana 47907, United States
- Pramey Upadhyaya Elmore Family School of Electrical and Computer Engineering, Purdue University, West Lafayette, Indiana 47907, United States
- Yong P. Chen Department of Physics and Astronomy, Purdue University, West Lafayette, Indiana 47907, United States; Elmore Family School of Electrical and Computer Engineering, Birck Nanotechnology Center, and Purdue Quantum Science and Engineering Institute, Purdue University, West Lafayette, Indiana 47907, United States
- Sunil A. Bhave Elmore Family School of Electrical and Computer Engineering and Birck Nanotechnology Center, Purdue University, West Lafayette, Indiana 47907, United States; Occid.org/0000-0001-7193-2241

Complete contact information is available at: https://pubs.acs.org/10.1021/acs.nanolett.1c02495

Notes

The authors declare no competing financial interest.

ACKNOWLEDGMENTS

T.L. thanks the Purdue Quantum Science and Engineering Institute (PQSEI) for support through the seed grant, the DARPA NLM program, and the DARPA QUEST program. We thank Yuan Ping and Vladimir M. Shalaev for helpful discussions. B.J. and S.A.B. are supported by National Science Foundation Award No. 1839164. A.E.L.A., M.A.S., Y.P.C., P.U., and A.B.S.'s contributions are based upon work supported by the U.S. Department of Energy, Office of Science, National Quantum Information Science Research Centers, Quantum Science Center.

■ REFERENCES

- (1) Togan, E.; Chu, Y.; Trifonov, A. S.; Jiang, L.; Maze, J.; Childress, L.; Dutt, M. G.; Sørensen, A. S.; Hemmer, P. R.; Zibrov, A. S.; et al. Quantum entanglement between an optical photon and a solid-state spin qubit. *Nature* **2010**, *466*, 730–734.
- (2) Bradley, C.; Randall, J.; Abobeih, M.; Berrevoets, R.; Degen, M.; Bakker, M.; Markham, M.; Twitchen, D.; Taminiau, T. A ten-qubit solid-state spin register with quantum memory up to one minute. *Phys. Rev. X* **2019**, *9*, 031045.
- (3) Dolde, F.; Fedder, H.; Doherty, M. W.; Nöbauer, T.; Rempp, F.; Balasubramanian, G.; Wolf, T.; Reinhard, F.; Hollenberg, L. C.; Jelezko, F.; et al. Electric-field sensing using single diamond spins. *Nat. Phys.* **2011**, *7*, 459–463.
- (4) Grinolds, M.; Warner, M.; De Greve, K.; Dovzhenko, Y.; Thiel, L.; Walsworth, R. L.; Hong, S.; Maletinsky, P.; Yacoby, A. Subnanometre resolution in three-dimensional magnetic resonance imaging of individual dark spins. *Nat. Nanotechnol.* **2014**, *9*, 279.
- (5) Schirhagl, R.; Chang, K.; Loretz, M.; Degen, C. L. Nitrogenvacancy centers in diamond: nanoscale sensors for physics and biology. *Annu. Rev. Phys. Chem.* **2014**, *65*, 83–105.
- (6) Thiel, L.; Wang, Z.; Tschudin, M. A.; Rohner, D.; Gutiérrez-Lezama, I.; Ubrig, N.; Gibertini, M.; Giannini, E.; Morpurgo, A. F.; Maletinsky, P. Probing magnetism in 2D materials at the nanoscale with single-spin microscopy. *Science* **2019**, *364*, 973–976.
- (7) Doherty, M. W.; Manson, N. B.; Delaney, P.; Jelezko, F.; Wrachtrup, J.; Hollenberg, L. C. The nitrogen-vacancy colour centre in diamond. *Phys. Rep.* **2013**, *528*, 1–45.
- (8) Gruber, A.; Dräbenstedt, A.; Tietz, C.; Fleury, L.; Wrachtrup, J.; Von Borczyskowski, C. Scanning confocal optical microscopy and magnetic resonance on single defect centers. *Science* **1997**, *276*, 2012–2014.
- (9) Koehl, W. F.; Buckley, B. B.; Heremans, F. J.; Calusine, G.; Awschalom, D. D. Room temperature coherent control of defect spin qubits in silicon carbide. *Nature* **2011**, *479*, 84–87.
- (10) Riedel, D.; Fuchs, F.; Kraus, H.; Väth, S.; Sperlich, A.; Dyakonov, V.; Soltamova, A.; Baranov, P.; Ilyin, V.; Astakhov, G. Resonant addressing and manipulation of silicon vacancy qubits in silicon carbide. *Phys. Rev. Lett.* **2012**, *109*, 226402.
- (11) Tran, T. T.; Wang, D.; Xu, Z.-Q.; Yang, A.; Toth, M.; Odom, T. W.; Aharonovich, I. Deterministic coupling of quantum emitters in 2D materials to plasmonic nanocavity arrays. *Nano Lett.* **2017**, *17*, 2634–2639.
- (12) Caldwell, J. D.; Aharonovich, I.; Cassabois, G.; Edgar, J. H.; Gil, B.; Basov, D. Photonics with hexagonal boron nitride. *Nature Reviews Materials* **2019**, *4*, 552–567.
- (13) Exarhos, A. L.; Hopper, D. A.; Patel, R. N.; Doherty, M. W.; Bassett, L. C. Magnetic-field-dependent quantum emission in hexagonal boron nitride at room temperature. *Nat. Commun.* **2019**, 10, 222.
- (14) Konthasinghe, K.; Chakraborty, C.; Mathur, N.; Qiu, L.; Mukherjee, A.; Fuchs, G. D.; Vamivakas, A. N. Rabi oscillations and resonance fluorescence from a single hexagonal boron nitride quantum emitter. *Optica* **2019**, *6*, 542–548.

- (15) Tran, T. T.; Bray, K.; Ford, M. J.; Toth, M.; Aharonovich, I. Quantum emission from hexagonal boron nitride monolayers. *Nat. Nanotechnol.* **2016**, *11*, 37–41.
- (16) Palombo Blascetta, N.; Liebel, M.; Lu, X.; Taniguchi, T.; Watanabe, K.; Efetov, D. K.; van Hulst, N. F. Nanoscale imaging and control of hexagonal boron nitride single photon emitters by a resonant nanoantenna. *Nano Lett.* **2020**, *20*, 1992–1999.
- (17) Gottscholl, A.; Kianinia, M.; Soltamov, V.; Orlinskii, S.; Mamin, G.; Bradac, C.; Kasper, C.; Krambrock, K.; Sperlich, A.; Toth, M.; et al. Initialization and read-out of intrinsic spin defects in a van der Waals crystal at room temperature. *Nat. Mater.* 2020, *19*, 540–545.
- (18) Mendelson, N.; Chugh, D.; Reimers, J. R.; Cheng, T. S.; Gottscholl, A.; Long, H.; Mellor, C. J.; Zettl, A.; Dyakonov, V.; Beton, P. H.; et al. Identifying carbon as the source of visible single-photon emission from hexagonal boron nitride. *Nat. Mater.* **2021**, *20*, 321–328.
- (19) Gottscholl, A.; Diez, M.; Soltamov, V.; Kasper, C.; Sperlich, A.; Kianinia, M.; Bradac, C.; Aharonovich, I.; Dyakonov, V. Room temperature coherent control of spin defects in hexagonal boron nitride. *Science Advances* **2021**, *7*, No. eabf3630.
- (20) Chejanovsky, N.; Mukherjee, A.; Geng, J.; Chen, Y.-C.; Kim, Y.; Denisenko, A.; Finkler, A.; Taniguchi, T.; Watanabe, K.; Dasari, D. B. R.; et al. Single-spin resonance in a van der Waals embedded paramagnetic defect. *Nat. Mater.* **2021**, *20*, 1079–1084.
- (21) Stern, H. L.; Jarman, J.; Gu, Q.; Barker, S. E.; Mendelson, N.; Chugh, D.; Schott, S.; Tan, H. H.; Sirringhaus, H.; Aharonovich, I.; et al. Room-temperature optically detected magnetic resonance of single defects in hexagonal boron nitride. 2021, arXiv:2103.16494. arXiv.org e-Print archive. https://arxiv.org/abs/2103.16494 (accessed August 12, 2021).
- (22) Gottscholl, A.; Diez, M.; Soltamov, V.; Kasper, C.; Krauße, D.; Sperlich, A.; Kianinia, M.; Bradac, C.; Aharonovich, I.; Dyakonov, V. Spin defects in hBN as promising temperature, pressure and magnetic field quantum sensors. *Nat. Commun.* **2021**, *12*, 4480.
- (23) Abdi, M.; Chou, J.-P.; Gali, A.; Plenio, M. B. Color centers in hexagonal boron nitride monolayers: a group theory and ab initio analysis. *ACS Photonics* **2018**, *5*, 1967–1976.
- (24) Ivády, V.; Barcza, G.; Thiering, G.; Li, S.; Hamdi, H.; Chou, J.-P.; Legeza, Ö.; Gali, A. Ab initio theory of the negatively charged boron vacancy qubit in hexagonal boron nitride. *npj Computational Materials* **2020**, *6*, 41.
- (25) Reimers, J. R.; Shen, J.; Kianinia, M.; Bradac, C.; Aharonovich, I.; Ford, M. J.; Piecuch, P. Photoluminescence, photophysics, and photochemistry of the $V_{\rm B}^-$ defect in hexagonal boron nitride. *Phys. Rev. B: Condens. Matter Mater. Phys.* **2020**, *102*, 144105.
- (26) Liu, W.; et al. Rabi oscillation of V_B^- spin in hexagonal boron nitride. 2021, arXiv:2101.11220. arXiv.org e-Print archive. https://arxiv.org/abs/2101.11220 (accessed August 12, 2021).
- (27) Kianinia, M.; White, S.; Froch, J. E.; Bradac, C.; Aharonovich, I. Generation of spin defects in hexagonal boron nitride. *ACS Photonics* **2020**, *7*, 2147–2152.
- (28) Gao, X.; Pandey, S.; Kianinia, M.; Ahn, J.; Ju, P.; Aharonovich, I.; Shivaram, N.; Li, T. Femtosecond Laser Writing of Spin Defects in Hexagonal Boron Nitride. *ACS Photonics* **2021**, *8*, 994–1000.
- (29) Murzakhanov, F. F.; Yavkin, B. V.; Mamin, G. V.; Orlinskii, S. B.; Mumdzhi, I. E.; Gracheva, I. N.; Gabbasov, B. F.; Smirnov, A. N.; Davydov, V. Y.; Soltamov, V. A. Creation of Negatively Charged Boron Vacancies in Hexagonal Boron Nitride Crystal by Electron Irradiation and Mechanism of Inhomogeneous Broadening of Boron Vacancy-Related Spin Resonance Lines. *Nanomaterials* **2021**, *11*, 1373
- (30) Abdi, M.; Hwang, M.-J.; Aghtar, M.; Plenio, M. B. Spin-Mechanical Scheme with Color Centers in Hexagonal Boron Nitride Membranes. *Phys. Rev. Lett.* **2017**, *119*, 233602.
- (31) Li, P.-B.; Zhou, Y.; Gao, W.-B.; Nori, F. Enhancing Spin-Phonon and Spin-Spin Interactions Using Linear Resources in a Hybrid Quantum System. *Phys. Rev. Lett.* **2020**, *125*, 153602.

- (32) Shimizu, K. T.; Woo, W. K.; Fisher, B. R.; Eisler, H. J.; Bawendi, M. G. Surface-Enhanced Emission from Single Semi-conductor Nanocrystals. *Phys. Rev. Lett.* **2002**, *89*, 117401.
- (33) Song, M.; Wu, B.; Chen, G.; Liu, Y.; Ci, X.; Wu, E.; Zeng, H. Photoluminescence plasmonic enhancement of single quantum dots coupled to gold microplates. *J. Phys. Chem. C* **2014**, *118*, 8514–8520.
- (34) Shalaginov, M. Y.; Bogdanov, S. I.; Lagutchev, A. S.; Kildishev, A. V.; Boltasseva, A.; Shalaev, V. M. On-Chip Single-Layer Integration of Diamond Spins with Microwave and Plasmonic Channels. *ACS Photonics* **2020**, *7*, 2018–2026.
- (35) Liu, W.; Li, Z.-P.; Yang, Y.-Z.; Yu, S.; Meng, Y.; Wang, Z.-A.; Li, Z.-C.; Guo, N.-J.; Yan, F.-F.; Li, Q.; Wang, J.-F.; et al. Temperature-dependent energy-level shifts of Spin Defects in hexagonal Boron Nitride. *ACS Photonics* **2021**, *8*, 1889–1895.
- (36) Lehtinen, O.; Dumur, E.; Kotakoski, J.; Krasheninnikov, A.; Nordlund, K.; Keinonen, J. Production of defects in hexagonal boron nitride monolayer under ion irradiation. *Nucl. Instrum. Methods Phys. Res., Sect. B* **2011**, *269*, 1327–1331.
- (37) Dréau, A.; Lesik, M.; Rondin, L.; Spinicelli, P.; Arcizet, O.; Roch, J.-F.; Jacques, V. Avoiding power broadening in optically detected magnetic resonance of single NV defects for enhanced dc magnetic field sensitivity. *Phys. Rev. B: Condens. Matter Mater. Phys.* **2011**, *84*, 195204.
- (38) Ye, M.; Seo, H.; Galli, G. Spin coherence in two-dimensional materials. *npj Computational Materials* **2019**, *5*, 44.
- (39) Akselrod, G. M.; Argyropoulos, C.; Hoang, T. B.; Ciracì, C.; Fang, C.; Huang, J.; Smith, D. R.; Mikkelsen, M. H. Probing the mechanisms of large Purcell enhancement in plasmonic nanoantennas. *Nat. Photonics* **2014**, *8*, 835–840.
- (40) Fröch, J. E.; Spencer, L.; Kianinia, M.; Totonjian, D.; Nguyen, M.; Gottscholl, A.; Dyakonov, V.; Toth, M.; Kim, S.; Aharonovich, I. Coupling spin defects in hexagonal boron nitride to monolithic bullseye cavities. *Nano Lett.* **2021**, *21*, 6549–6555.

Supporting Information:

High-contrast plasmonic-enhanced shallow spin defects in hexagonal boron nitride for quantum sensing

Xingyu Gao,[†] Boyang Jiang,[‡] Andres E. Llacsahuanga Allcca,[†] Kunhong Shen,[†] Mohammad A. Sadi,[‡] Abhishek B. Solanki,[‡] Peng Ju,[†] Zhujing Xu,[†] Pramey Upadhyaya,[‡] Yong P. Chen,^{†,‡,¶,§} Sunil A. Bhave,^{‡,¶} and Tongcang Li*,^{†,‡,¶,§}

†Department of Physics and Astronomy, Purdue University, West Lafayette, Indiana 47907, USA

‡Elmore Family School of Electrical and Computer Engineering, Purdue University, West

Lafayette, Indiana 47907, USA

¶Birck Nanotechnology Center, Purdue University, West Lafayette, IN 47907, USA §Purdue Quantum Science and Engineering Institute, Purdue University, West Lafayette, Indiana 47907, USA

E-mail: tcli@purdue.edu

Methods

Preparation of hBN spin defects: We used commercially available hBN single crystals purchased from 2D Semiconductors. hBN nanosheets were exfoliated to 10-100 nm thick with tapes and put on top of a 1 cm×1 cm Si substrate. The sample was put into a home-

built ion implanter based on the ion source ISIS3000 (PSP Vacuum Technology). The hBN flakes were implanted with low-energy He⁺ ions ranging from 200 eV to 3 keV.

Pick up and transfer hBN flakes: After ion implantation, hBN flakes were transferred onto other substrates (e.g. sapphire, gold, etc.) for further measurement. In order to pick up and transfer the hBN flakes, we use a stamp consisting of a thin film of polycarbonate (PC) mounted on a block of polydimethylsiloxane (PDMS) for mechanical support. The stamp is placed on a glass slide attached to a micromanipulator under a microscope (2D) Heterostructure Transfer System, hq graphene). The Si substrate, with hBN flakes to be transferred, is fixed onto a heated stage and positioned with a micromanipulator. The PC stamp is first placed into contact with a selected hBN flakes. Then the stage is heated up and let it gradually cool down after reaching 150 °C. Next, we lift the PC stamp from the Si substrate at 60 °C. These temperatures are chosen because they allow us to pick up the hBN flakes with a 100% success rate. Then we remove the Si substrate and place the target substrate (gold, sapphire, etc) onto the heated stage. We position the hBN flakes over a selected region of the target substrate (e.g. center part of the gold microstrip), and bring the PC stamp and target substrate fully into contact. Again, the stage is heated up to 150 °C and then let it gradually cool down. At 60 °C, we lift the glass slide with PDMS block. The PC stamp remains on the target substrate due to the preferential adhesion. Finally, we use chloroform, acetone and isopropyl alcohol to dissolve the PC stamp and clean the substrate surface.

Confocal microscope: Optical measurements were carried out at room temperature under ambient conditions using a home-built confocal microscope system. A 532-nm laser was sent through a 650 nm dichroic mirror and focused on the sample using an high numerical aperture (NA=0.9) objective lens with 100X magnification. An acousto optic modulator (ISOMET, M1205-T110L-1) was used as an fast optical switch. The PL was separated from the laser by a dichroic mirror and the residual laser light was aborbed by two 550-nm long-pass filters.

Afterward, the PL was coupled into a 125-um single-mode fiber, and guided to a single photon counter (Excelitas, SPCM-AQRH) or a spectrometer (Andor shamrock SR-500).

Optically Detected Magnetic Resonance Measurements: ODMR measurements were performed using the confocal system described above. A gold microwave coplanar waveguide (Figure S1) was patterned using standard photolithography techniques and electron beam evaporation of 300 nm Au on sapphire. A 10 nm Ti layer is deposited on sapphire before Au deposition. The root-mean-square (rms) roughness of the gold film is measured to be 1.2 nm (Figure S1(b)). The width of the center microstrip line is 50 μ m to deliver the microwave to the hBN samples on top of it. Two fast RF switches (Mini-Circuits ZASWA-2-50DRA+) were used to modulate the microwave amplitude for detecting the change of PL intensities. A permanent magnet was mounted on a linear translation stage behind the sample to apply a tunable external dc magnetic field perpendicular to the hBN flake surface.

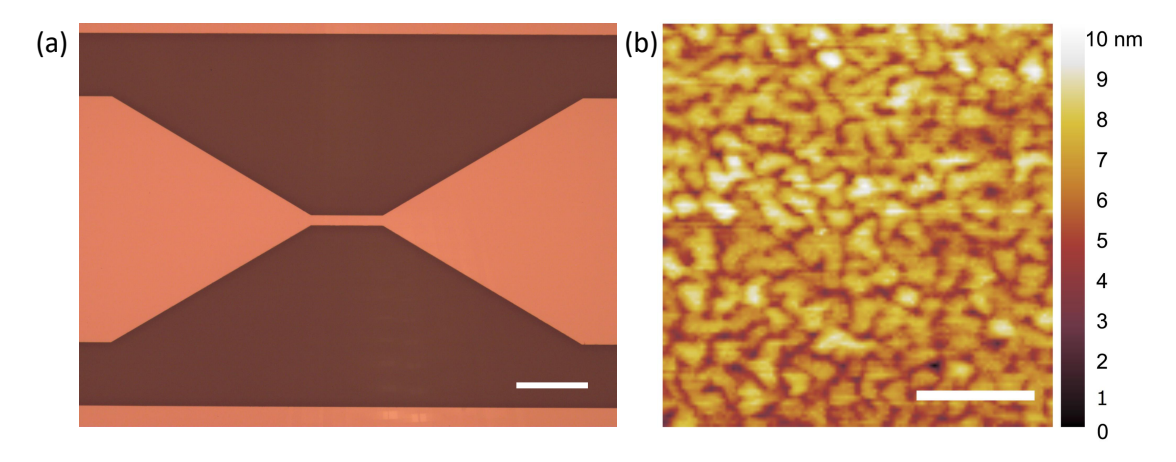


Figure S1: (a) The optical image of the gold waveguide. Scale bar: 300 μ m. (b) The AFM image of the gold film of the waveguide. Scale bar: 400 nm.

Effects of ion implantation energy and dose

Experimentally, we have successfully generated V_B^- defects with an ion energy as low as 200 eV, corresponding to a depth around 2.5 nm. When the dose density is fixed at 5×10^{13}

cm⁻² for implantation, the PL intensity increases when we increase the ion energy (Fig. S2(a)), implying that ions with higher energies have a larger probability to break the B–N bonds and create V_B^- defects.

In addition, we study the dependence of the PL intensity on the He⁺ dose. We fix the ion energy and tune the implantation duration to change the dose (Fig. S2(b)). The PL intensity first increases with the increasing implantation dose, and then becomes saturated at a high dose. The implantation with 600 eV He⁺ ions has a lower saturation dose and PL intensity than those with 2.5 keV He⁺ ions. This is because the implantation depth of low-energy ions is smaller than that of high-energy ions.

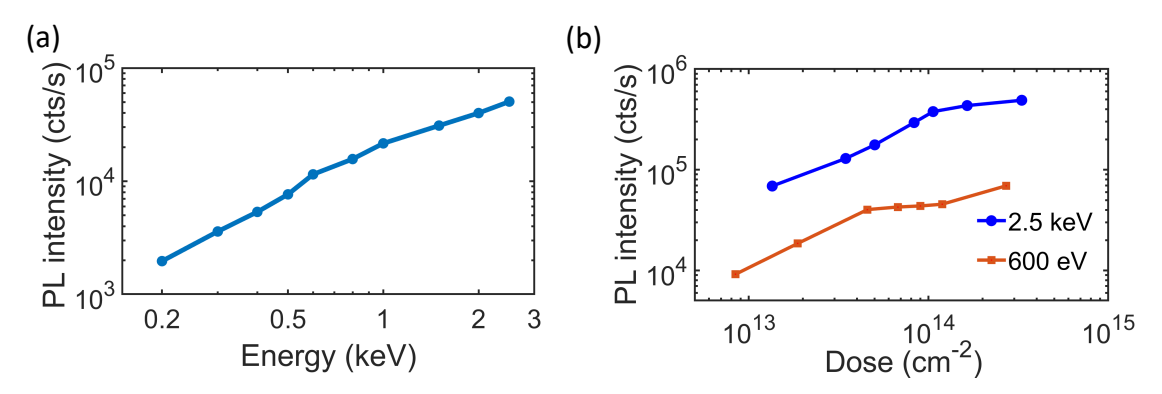


Figure S2: (a) PL intensity as a function of the $\mathrm{He^+}$ ion energy. The dose density is fixed at 5×10^{13} cm⁻². A 3 mW 532-nm laser is used for excitation. (b) PL intensity with different ion implantation doses.

Measurement of the electron spin initialization time

We also characterize the electron spin initialization time as a function of the power of the 532 nm excitation laser. Figure S3 presents time-resolved photon count rates beginning with different spin states. The initial state is a mixture state at thermal equilibrium when the laser has been off for a long time (much longer than T_1). When the laser pulse is turned on, the electron spins are getting polarized and the photon count rate increases. To prepare the polarized state as a reference, we apply a 3- μ s-length laser pulse to polarize electron spins to the $m_s = 0$ state. The laser is turned off for 100 ns (which is much shorter than T_1) before

being turned on again for recording the reference photon count rate. The difference between the count rates of these two states is calculated and then fitted exponentially to determine the spin initialization time. We find that the required spin initialization time is on the order of 100 ns. The gold film reduces the spin initialization time, which also speeds up quantum sensing.

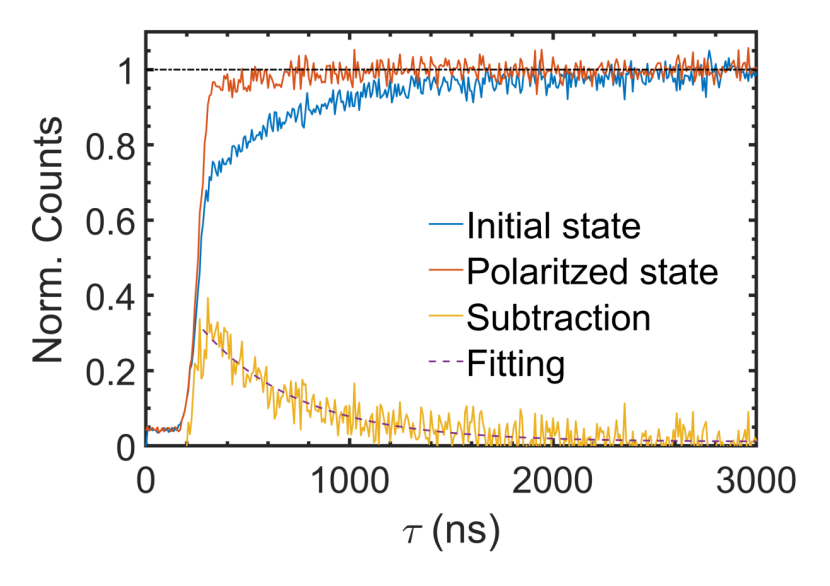


Figure S3: Time-resolved photon counts starting from different spin states. The laser power is set as 200 μ W.

Enhancement of the brightness with different substrates

In the main text, we reported the PL enhancement due to the gold film. Here we compare the brightness of the V_B^- on different substrates (Fig. S4). We use the same photolithography method to fabricate a 300-nm thick silver microstrip on top of the sapphire wafer. Then we transfer the ion implanted hBN flakes onto both the silver and sapphire substrates. On the silver film, we also observed a comparable brightness enhancement (up to 16 times) as the gold film. Besides, we also compare the brightness of V_B^- on SiO₂ and indium tin oxide (ITO). No brightness enhancement is observed on either SiO₂ or ITO substrates.

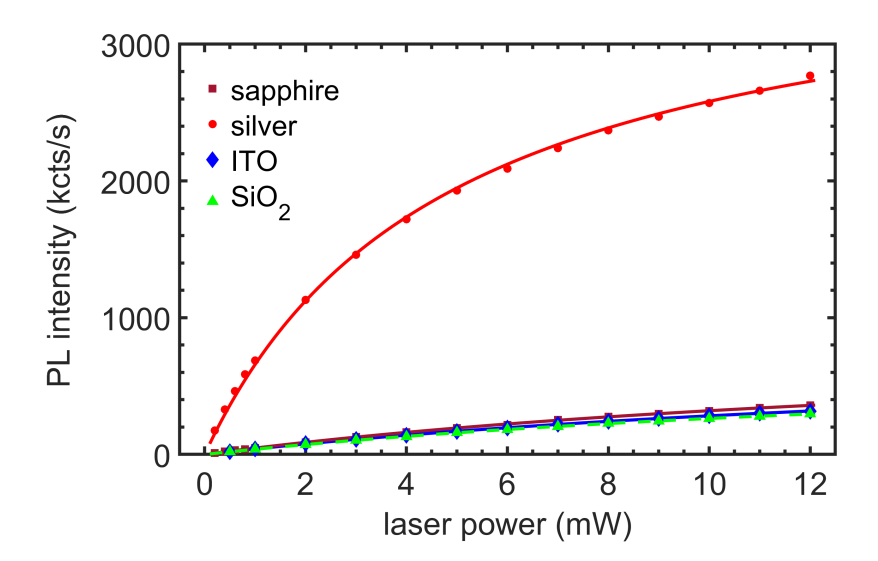


Figure S4: V_B^- PL intensities as functions of the laser power on different substrates. Sapphire, silver, ITO and SiO₂ substrates are studied here for comparison. V_B^- on the silver substrate has a similar brightness enhancement as the V_B^- on the gold. Other substrates studied here do not show observable brightness enhancement. The V_B^- defects are generated by 2.5 keV He⁺ ions.

Analysis of ODMR contrasts, lineshapes and sensitivity

Fit to the ODMR lineshape: Here we use a double Lorentzian model to fit the ODMR spectra, and determine the ODMR contrasts and lineshapes. The intensity of the ODMR spectrum as a function of the microwave frequency ν can be written as ²

$$I(\nu) = R \left[1 - C_1 \frac{(\Delta \nu_1/2)^2}{(\nu - \nu_1)^2 + (\Delta \nu_1/2)^2} - C_2 \frac{(\Delta \nu_2/2)^2}{(\nu - \nu_2)^2 + (\Delta \nu_2/2)^2} \right],\tag{1}$$

where R is the photon count rate, C_i (i=1,2) is the ODMR contrast associated to the dip of the PL intensity, ν_i (i=1,2) is the associated central resonance frequency and $\Delta\nu_i$ (i=1,2) is the associated linewidth (FWHM). An external magnetic field will induce a shift of the central frequency ν_i (i=1,2) through the Zeeman effect.

Magnetic field Sensitivity with CW ODMR: To measure an external dc magnetic field, we can directly evaluate the Zeeman shifts in the CW ODMR spectrum. The sensitivity in

this is determined by the PL intensity, contrast and linewidth, which reads as³

$$\eta_B = A \times \frac{h}{g\mu_B} \times \frac{\Delta\nu}{C\sqrt{R}},\tag{2}$$

where h is the Planck constant, g is the Landé g-factor and μ_B is the Bohr magneton. In this expression, A is a numerical parameter related to the specific lineshape function. For a Lorentzian profile that we used above, A ≈ 0.77 .

The effect of the microwave power on ODMR contrasts and linewidths: In the main text, we show the microwave power P_{MW} dependence of the ODMR contrast and linewidth. We fit the ODMR signal to a double lorentzian model at different microwave powers P_{MW} . Then the contrasts and linewidths are fit to³

$$C(P_{MW}) = C_0 \times \frac{P_{MW}}{P_{MW} + B},\tag{3}$$

and

$$\Delta\nu(P_{MW}) = D_1 \times \sqrt{P_{MW} + D_2},\tag{4}$$

respectively. Here B, D_1 and D_2 are the fitting parameters that relate to the spin polarization rates, optical satuation parameters and the rates of optical cycles.

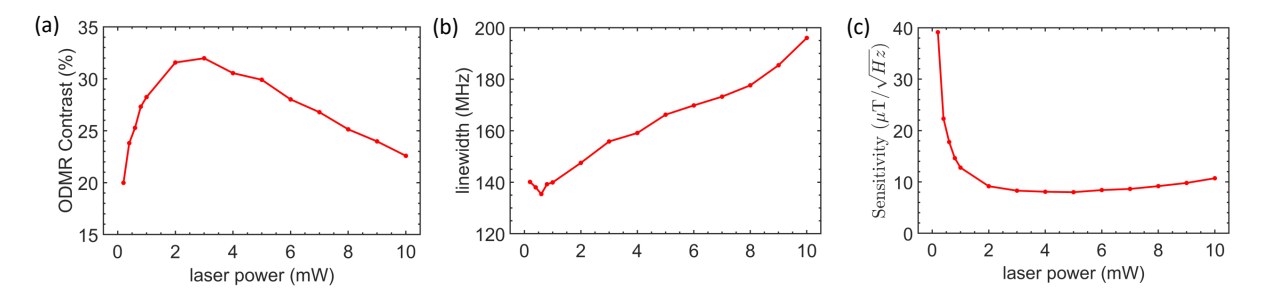


Figure S5: Laser power dependence of CW ODMR measurements. The microwave power is fixed at 0.4 W. (a) ODMR contrast (b) ODMR linewidth (c) Magnetic field sensitivity based on the contrast, linewidth and PL intensity.

The effect of the laser power on ODMR contrasts and linewidths: Here we also perform a group of ODMR experiments to determine the optimal laser power for getting a high magnetic-field sensitivity (Fig. S5). When we increase the laser power from 200 μ W to 10 mW, the ODMR contrast first increases and then decreases after reaching the maxima. Meanwhile, the ODMR linewidth keeps increasing. According to Eq. 2, the sensitivity is proportional to $\frac{\Delta\nu}{C\sqrt{R}}$. Thus, besides the contrast and linewidth, the excitation laser power affects the sensitivity also through the PL count rate R. When we increase the laser power, the PL intesity also significantly increases before reaching the saturation power. As a result, we find that 5 mW laser in our case is around the optimal condition.

The effect of a different microwave alignment: We also designed a Ω -shaped microwave waveguide to apply the microwave (Figure S6(a)). The magnetic field of the driving microwave is nearly perpendicular to the hBN flake at the center of the Ω ring. Under 1 mW laser excitation and 2.5 W microwave driving, the CW ODMR contrast is around 7.5%, which is about 6 times smaller than what we observed when microwave field is aligned correctly (e.g. when the hBN flake is on a straight-stripe waveguide in Fig. S1).

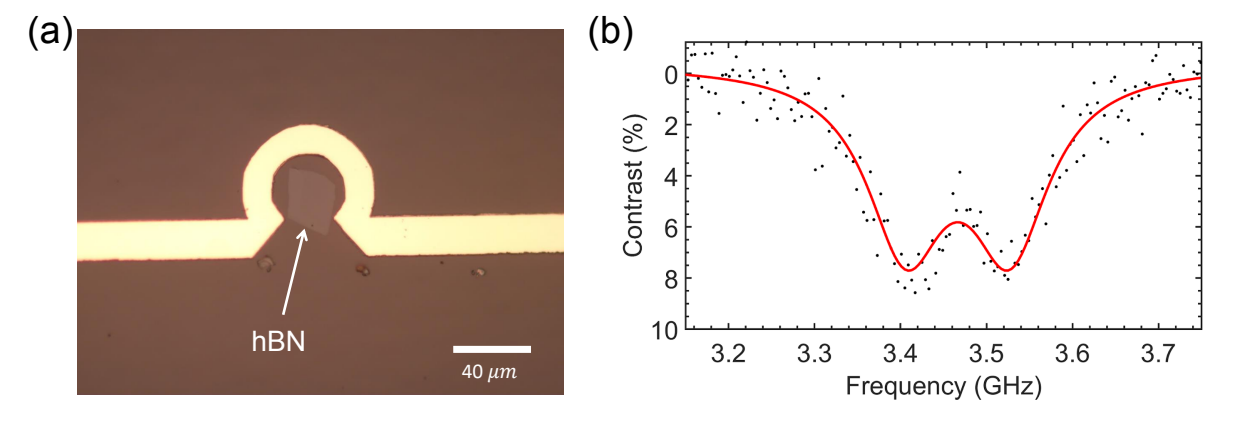


Figure S6: CW ODMR with a Ω -shaped microwave waveguide . (a) Image of a hBN flake inside the Ω ring. In this geometry, the magnetic field of the microwave is approximately perpendicular to the flake's surface. The width of the straight (horizontal) gold line is 20 μ m. The outer radius of the Ω ring is 35 μ m and the inner radius of the ring is 20 μ m. (b) ODMR spectrum under 1 mW laser excitation and 2.5 W microwave driving.

High-contrast CW ODMR with no plasmonic enhancement: To confirm that the high contrast of the CW ODMR is not due to the plasmonic enhancement but the result of the intrinsic property of V_B^- defects, we choose a thick hBN flake to perform the CW ODMR measurements. The hBN flake is a few hundred nm thick so that we do not observe any PL enhancement. The CW ODMR measurements show that the high contrast from the V_B^- defects does not rely on the plasmonic effect (Figure S7).

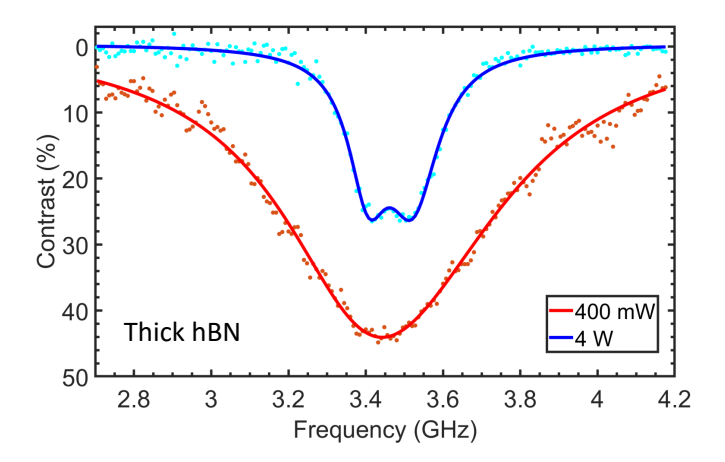


Figure S7: High-contrast CW ODMR of hBN V_B^- defects in a thick hBN flake on a gold straight-stripe waveguide. The hBN flake chosen here is a few hundred nm thick and has no plasmonic enhancement on the PL intensity.

References

- (1) Purdie, D.; Pugno, N.; Taniguchi, T.; Watanabe, K.; Ferrari, A.; Lombardo, A. Cleaning interfaces in layered materials heterostructures. *Nature communications* **2018**, *9*, 5387.
- (2) Jensen, K.; Acosta, V.; Jarmola, A.; Budker, D. Light narrowing of magnetic resonances in ensembles of nitrogen-vacancy centers in diamond. *Physical Review B* 2013, 87, 014115.
- (3) Dréau, A.; Lesik, M.; Rondin, L.; Spinicelli, P.; Arcizet, O.; Roch, J.-F.; Jacques, V. Avoiding power broadening in optically detected magnetic resonance of single NV defects for enhanced dc magnetic field sensitivity. *Physical Review B* 2011, 84, 195204.